

Identifying the Active Surfaces of Electrochemically Tuned LiCoO_2 for Oxygen Evolution Reaction

Zhiyi Lu,[†] Guangxu Chen,[†] Yanbin Li,[†] Haotian Wang,[‡] Jin Xie,[†] Lei Liao,[†] Chong Liu,[†] Yayuan Liu,[†] Tong Wu,[†] Yuzhang Li,[†] Alan C. Luntz,[§] Michal Bajdich,^{*,§,||} and Yi Cui^{*,†,⊥}

[†]Department of Material Science and Engineering, Stanford University, Stanford, California 94305, United States

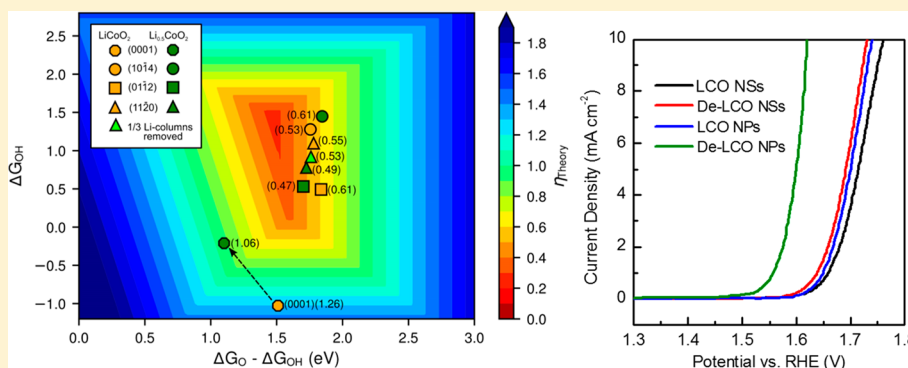
[‡]Rowland Institute, Harvard University, Cambridge, Massachusetts 02142, United States

[§]SUNCAT Center for Interface Science and Catalysis, Chemical Engineering, Stanford University, Stanford, California 94305, United States

^{||}SLAC National Accelerator Laboratory, 2575 Sand Hill Road, Menlo Park, California 94025, United States

[⊥]Stanford Institute for Materials and Energy Science, SLAC National Accelerator Laboratory, Menlo Park, California 94025, United States

Supporting Information



ABSTRACT: Identification of active sites for catalytic processes has both fundamental and technological implications for rational design of future catalysts. Herein, we study the active surfaces of layered lithium cobalt oxide (LCO) for the oxygen evolution reaction (OER) using the enhancement effect of electrochemical delithiation (De-LCO). Our theoretical results indicate that the most stable (0001) surface has a very large overpotential for OER independent of lithium content. In contrast, edge sites such as the nonpolar (1120) and polar (0112) surfaces are predicted to be highly active and dependent on (de)lithiation. The effect of lithium extraction from LCO on the surfaces and their OER activities can be understood by the increase of Co^{4+} sites relative to Co^{3+} and by the shift of active oxygen 2p states. Experimentally, it is demonstrated that LCO nanosheets, which dominantly expose the (0001) surface show negligible OER enhancement upon delithiation. However, a noticeable increase in OER activity (~ 0.1 V in overpotential shift at 10 mA cm^{-2}) is observed for the LCO nanoparticles, where the basal plane is greatly diminished to expose the edge sites, consistent with the theoretical simulations. Additionally, we find that the OER activity of De-LCO nanosheets can be improved if we adopt an acid etching method on LCO to create more active edge sites, which in turn provides a strong evidence for the theoretical indication.

INTRODUCTION

Layered materials have attracted increasing attention owing to their strong anisotropic effect on the basal and edge planes, endowing these materials with novel chemical and physical properties.^{1–3} In particular, transition-metal dichalcogenides (TMDs) are becoming the focus of fundamental research due to their tunable chemical compositions that lead to wide-ranging applications.^{4–9} One typical example is molybdenum disulfide, whose edge plane possesses a high activity for hydrogen evolution reaction due to the appropriate binding energy toward proton.^{10,11} Layered transition-metal oxyhydroxides (MOOH_x , $M = \text{Ni/Fe, Co, Mn}$) are another class of

layered materials known to be one of the most active OER catalysts under alkaline conditions.^{12–14} Similar to TMDs, edge sites as opposed to more abundant basal plane sites have been found to be the OER active centers for the oxyhydroxides. Therefore, identifying the OER active surfaces and sites is of great interest to both experimental and theoretical investigations. Such understanding is also necessary for further increasing the concentration and enhancing the activity of

Received: March 15, 2017

Published: April 18, 2017



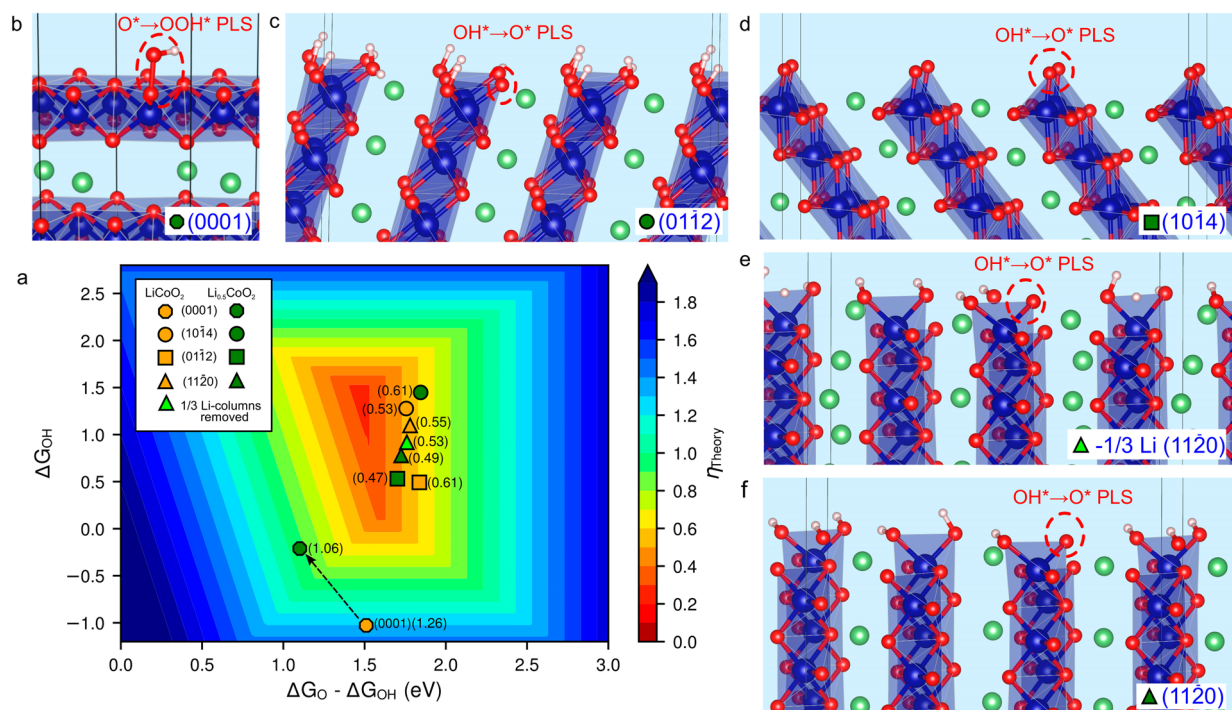


Figure 1. (a) Calculated OER activity map of the $\text{LiCoO}_2/\text{Li}_{0.5}\text{CoO}_2$ system. The orange (green) symbols position the activity of individual surface of LiCoO_2 ($\text{Li}_{0.5}\text{CoO}_2$) with the value of theoretical OER overpotential (η_{Theory}) shown in brackets. The arrows indicate the change in the activity upon delithiation. (b–f) The structures of considered surfaces of $\text{Li}_{0.5}\text{CoO}_2$ with highlighted OER intermediates at the end of a potential-limiting step (PLS).

active sites, which is the next big challenge in the catalyst design.

Previous studies have shown that OER activity strongly depends on the type, coverage, and lattice strain of the exposed surface for Co_3O_4 ,¹⁵ CoOOH ,¹⁶ Ni-FeOOH ,^{17,18} and NCoO_x ($N = \text{La, Sr}$).^{19,20} Our previous experimental studies have demonstrated a general approach of electrochemical tuning of chemical and physical properties of the existing catalysts in organic electrolyte with a wide thermodynamic range.^{21–25} One representative example is LCO, which can be converted to Li_xCoO_2 ($x \approx 0.5$, De-LCO) by tuning the chemical potential to 4.3 V vs Li^+/Li along with significantly enhanced OER activity.²⁶ As LCO attains high crystallinity with multiple surfaces exposed under OER conditions,²⁷ it is intriguing to study the dependence of different surfaces and sites on LCO and De-LCO with respect to the OER activity.

The current investigation starts with a computational OER study, which demonstrates that two stable surfaces, (11 $\bar{2}$ 0) and (01 $\bar{1}$ 2), are likely responsible for the OER activity, while the (0001) surface is the most inactive one. This effect is attributed to the increased concentration of Co^{4+} sites as well as the associated shifting of 2p states of the active oxygen atoms. To confirm these predictions, we have experimentally synthesized two different morphologies of LCO with different distributions of the active surfaces: LCO nanosheets (LCO NSs) with dominantly basal (0001) surface exposure and LCO nanoparticles (LCO NPs) where the basal planes are drastically reduced to expose more edge sites. Our electrochemical results show that the delithiation treatment has negligible effect on the OER activity of the crystalline LCO NSs, while LCO NPs exhibit a noticeable enhancement. Together with the theoretical predictions, these experimental results confirm that the basal surface of De-LCO is very inactive for OER, while other major

surfaces, especially the (01 $\bar{1}$ 2) and (11 $\bar{2}$ 0), are active. Based on both theoretical indication and experimental demonstration, we have employed an acid etching methodology on LCO NSs to expose more active surfaces and improve OER activity, further supporting our hypothesis.

RESULTS AND DISCUSSION

The stoichiometric LCO crystallizes in a layered structure with alternating Li and O–Co–O layers along the [0001] direction. Due to a shift in stacking of the layers, the system has overall rhombohedral structure with $R\bar{3}m$ symmetry. LCO has multiple surfaces, and we choose 4 major surfaces, the polar (0001) and (01 $\bar{1}$ 2) and the nonpolar (10 $\bar{1}$ 4) and (11 $\bar{2}$ 0), for investigation. In the previous theoretical work, Kramer and Ceder studied the stability and surface reconstruction of the same surfaces under oxidizing conditions.²⁷ Here the OER activities and the surface stabilities of above surfaces for both the LCO and delithiated material ($\text{Li}_{0.5}\text{CoO}_2$) were studied by a computational simulation.

To assess the OER activity in this system, we have performed the DFT+U calculations of the theoretical OER overpotential, η_{Theory} for each individual surface (for details refer to the [Theoretical Section](#) and SI). According to a standard method, which has been applied to a large number of metal oxides,^{16,17,28,29} this purely thermodynamic approach requires the calculation of the free energy of adsorption, ΔG , of OH^* , O^* , and OOH^* intermediates on the surface under OER conditions, that is, at applied voltage above $U_{\text{RHE}} = 1.23$ V. Assuming the typical $4 e^-/\text{H}^+$ step OER mechanism with OOH^* step, the pH independent theoretical overpotential is easily obtained as

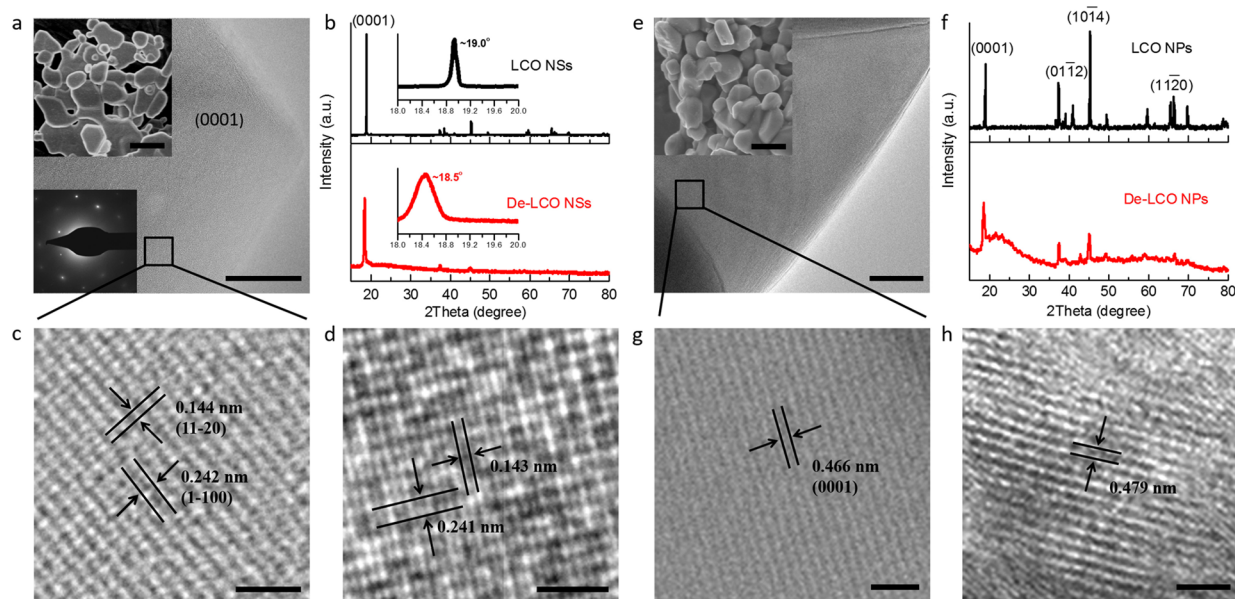


Figure 2. (a) Representative TEM image of LCO NSs, scale bar = 20 nm; the insets are the SEM image and SAED image of LCO NSs, demonstrating its sheet-like morphology with preferentially exposed (0001) surface, scale bar = 2 μm . (b) Powder XRD patterns of LCO NSs and De-LCO NSs; the insets are the localized XRD patterns within the 2θ range from 18° to 20° ; the negative shifting of the diffraction angle indicates the success of the delithiation process. (c, d) High resolution TEM images of LCO NSs before and after delithiation, respectively, suggesting that the lattice parameters of (0001) surface are not affected by the delithiation process, scale bar = 1 nm. (e) TEM image of LCO NPs, scale bar = 20 nm; the inset is the SEM image; this particle-like morphology indicates the LCO NPs expose random surfaces, scale bar = 500 nm. (f) Powder XRD patterns of LCO NPs and De-LCO NPs. (g, h) High resolution TEM images of LCO NPs before and after delithiation, respectively; the observation of (0001) lattice distance directly proves the surfaces perpendicular to this direction are exposed and the lattice distance along (0001) surface is enlarged by $\sim 3\%$, corresponding well with the XRD patterns, scale bar = 2 nm.

$$\eta_{\text{Theory}} = \max[\Delta G_{\text{OH}^*}, \Delta G_{\text{O}^*} - \Delta G_{\text{OH}^*}, \Delta G_{\text{OOH}^*} - \Delta G_{\text{O}^*}, 4.96 \text{ eV} - \Delta G_{\text{OOH}^*}] / e - 1.23 \text{ V} \quad (1)$$

Naturally, the step with the largest value in the eq 1 is referred as the potential-limiting step (denoted as “PLS”). The theoretical overpotential is calculated self-consistently at a surface coverage of O^* or OH^* species determined from surface Pourbaix diagram (Figure S1) at the same overpotential.

Our calculated results for the LCO and De-LCO (studied as $\text{Li}_{0.5}\text{CoO}_2$) are summarized in Figure 1. We have calculated the theoretical overpotentials for two polar surfaces, (0001) and (01 $\bar{1}2$), and two nonpolar surfaces, (10 $\bar{1}4$) and (11 $\bar{2}0$), for the LCO and De-LCO. We observe that the oxygen terminated (0001) surface of LCO is clearly the least active surface. In contrast, the OH covered (01 $\bar{1}2$) surface has a much better overpotential of 0.61 V and 1 ML OH covered (11 $\bar{2}0$) has an even better calculated overpotential of 0.55 V. However, a well-known stable surface of LCO, the 1 ML OH covered (10 $\bar{1}4$) is calculated to show the best activity with overpotential of only 0.53 V. Next, we have studied the effect of the delithiation process, which appeared as the moderate shift to the left in the $\Delta G_{\text{O}} - \Delta G_{\text{OH}}$ descriptor (x -axis) for most of the surfaces under consideration. Because of this shift, the overpotentials of (01 $\bar{1}2$) and (11 $\bar{2}0$) surfaces improve from 0.61 to 0.47 V and 0.55 to 0.49 V, respectively. However, it is observed that the overpotential of (10 $\bar{1}4$) surface is slightly worse (0.62 V) than the value (0.53 V) before delithiation. The (0001) surface still remains very inactive with overpotential greater than 1 V. Therefore, from this theoretical perspective, we believe the (11 $\bar{2}0$) and (01 $\bar{1}2$) surfaces are responsible for the enhanced OER activity of LCO after delithiation.

The above results for the theoretical OER activities of LCO and De-LCO are very intriguing for several reasons. First, all surfaces have the same PLS as $\text{OH}^* \rightarrow \text{O}^*$ and are therefore always on the right leg of the theoretical volcano plot (Figure 1a and Figure S2) except for the (0001) surface, which binds the intermediate too strong. Consequently, the $\Delta G_{\text{O}} - \Delta G_{\text{OH}}$ descriptor uniquely defines their activity. Second, we find that the (10 $\bar{1}4$), (11 $\bar{2}0$), and (01 $\bar{1}2$) surfaces under OER conditions are always covered with OH^* intermediate (Figure S1). This is quite surprising considering the high stability of clean nonpolar (10 $\bar{1}4$) and (11 $\bar{2}0$) surfaces.²⁷ These findings are also very important for understanding the effect of the delithiation, which will be discussed next.

Upon delithiation, the LCO undergoes a well-known elongation in the c lattice parameter (from $c = 14.158$ to $c = 14.610$ Å) and a slight contraction in the a lattice parameter (from $a = 2.834$ to $a = 2.816$ Å).³⁰ Electronically, LCO is a nonmagnetic Co^{3+} ($S = 0$) semiconductor with moderate band gap of ~ 2 eV. This changes to a mixture of Co^{3+} ($S = 0$) and Co^{4+} ($S = 1/2$) for De-LCO, which has a smaller band gap of ~ 1 eV (Figure S3).³¹ We believe that such a reduction in band gap can lead to an improvement of the electrochemical performance. The valence and conduction states near the Fermi level have about equal character of $\text{Co}(3d)$ and $\text{O}(2p)$ states, indicating the highly covalent nature of this system.³² The delithiation process of LCO has similar effects on its surfaces (Figure S4). As we have already established, the exposed surfaces of LCO under OER conditions are covered by OH adsorbates, which is also indicative by the presence of the less stable surface Co^{4+} species. The delithiation process leads to further increase of the Co^{4+} concentration in the subsurface and bulk regions of De-LCO.^{33,34} The surface Pourbaix surface

analysis (Figure S1) further reveals that the De-LCO surfaces require higher applied voltages than LCO to undergo transitions from clean \rightarrow OH* and from OH* \rightarrow O*. This comparison shows that De-LCO surfaces are harder to oxidize than LCO surfaces.

The OER activities of the (10 $\bar{1}$ 4), (11 $\bar{2}$ 0), and (01 $\bar{1}$ 2) surfaces are defined by the $\Delta G_{\text{O}} - \Delta G_{\text{OH}}$ energetics at the active site. For these surfaces, the active site has Co⁴⁺ character with OH* cover. Additionally, each active site is surrounded by other Co⁴⁺ sites at the surface and Co³⁺ sites in the subsurface. For De-LCO, the difference from LCO is that most of the subsurface Co³⁺ neighbors are further oxidized to Co⁴⁺. This change also has a direct effect on the O(2p) states, indicated by the presence of extra antibonding orbitals right above the Fermi level (Figure S4). We argue that the combined effect of more Co⁴⁺ neighbors and consequent shift of the O(2p) reduces the value of $\Delta G_{\text{O}} - \Delta G_{\text{OH}}$. Interestingly, for bulk systems, the exact same fingerprint in the O(2p) states for the higher oxidation of LCO was observed experimentally.³⁵ Lastly, we have verified that the shift in the $\Delta G_{\text{O}} - \Delta G_{\text{OH}}$ energies is not due to 3% expansive strain of *c*-lattice of LCO relative to De-LCO lattice. On the other hand, partial removal of 1/3 of Li atoms from LCO does improve $\Delta G_{\text{O}} - \Delta G_{\text{OH}}$ energy at the (11 $\bar{2}$ 0) surface (shown as light green triangle in Figure 1).

To experimentally investigate this surface effect on the De-LCO for OER, we have first synthesized single crystalline LCO NSs with average size and thickness of ~ 2 μm and ~ 150 nm, respectively, as shown in Figure 2a. Figure 2b shows that all the reflection lines in the XRD pattern of LCO NSs (black line) can be indexed to LiCoO₂ (JCPDS 36-1004), while the diffraction peak located at $2\theta \approx 19^\circ$ was unusually strong, demonstrating a preferential exposure of (0001) plane.^{36,37} The De-LCO NSs obtained by an electrochemical delithiation process of pristine LCO NSs (Figure S5) showed a monoclinic phase with a noticeable shift on the peak position of (0001) plane (the red line and inset of Figure 2b), which meant that half of the lithium was extracted and a new formula (Li_{0.5}CoO₂) was formed.^{38,39} It should be noted that the (0001) peak intensity of De-LCO NSs was still the highest, and the sheet-like morphology was mostly preserved even after delithiation, suggesting that the preferential orientation still existed (Figure S6). Closer inspection of the high resolution transmission electron microscopy image (HRTEM, Figure 2c) shows two typical lattice spacings (0.144 and 0.242 nm), which corresponded to (11 $\bar{2}$ 0) and (1 $\bar{1}$ 00) planes of LCO, respectively, thereby revealing that the preferentially exposed plane on LCO NSs was (0001). The delithiation process did not affect the crystal structure and symmetry of the (0001) plane with the negligible change on the lattice parameters of De-LCO (Figure 2d).

Besides the LCO NSs, LCO NPs (~ 400 nm) that expose random surfaces have also been fabricated (Figure 2e). The XRD pattern shows that most of the diffraction peaks have normal positions (black line in Figure 2f), while the (0001) peak intensity was greatly diminished. The intensity ratio between the theoretically predicted inactive (0001) surface and active (01 $\bar{1}$ 2) and (11 $\bar{2}$ 0) surfaces was dramatically changed from 67.1:1:2.4 to 2.9:1:1.4. Moreover, the lattice spacing of (0001) direction can be clearly observed in the representative HRTEM image (Figure 2g), directly proving that the surfaces perpendicular to this direction, such as (11 $\bar{2}$ 0), were exposed. The successful phase transformation after delithiation was also demonstrated by the XRD pattern (red line in Figure 2f) as

well as the lattice parameter change (from 0.466 to 0.479 nm, $\sim 3\%$ enlargement) shown in Figure 2h, while the morphology was still retained after electrochemical tuning (Figure S7).

The above results indicate that the as-synthesized LCO NSs preferentially expose the basal plane surface, while the LCO NPs have more randomized surface distribution. According to our simulation results, it is expected that the OER activity of LCO NPs would show a significant improvement after delithiation, while very little OER improvement is expected for LCO NSs. The OER catalytic activities of the LCOs as well as the corresponded De-LCOs were evaluated by steady-state electrochemistry measurements in a 0.1 M KOH aqueous solution using a typical three-electrode cell setup, and all the data have been corrected with a resistance drop of ~ 20 Ω . Figure 3a shows the typical polarization curves of four catalysts,

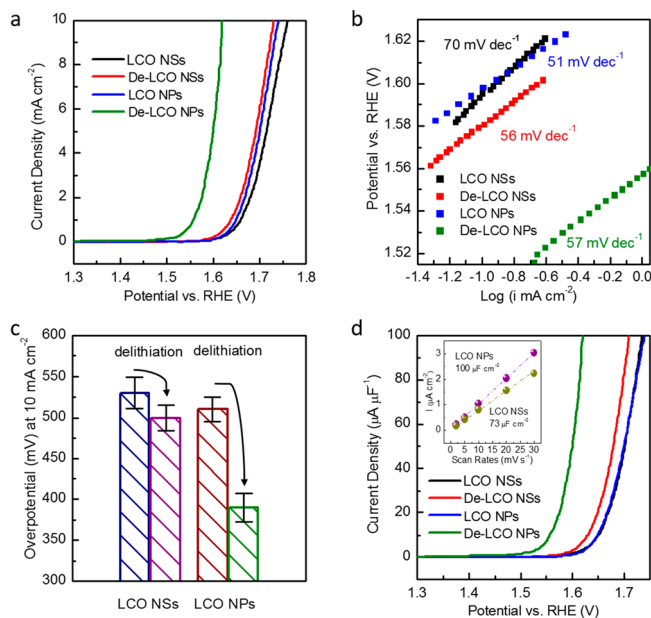


Figure 3. (a) Polarization curves of LCO NSs and NPs before and after delithiation, respectively. After delithiation, the LCO NPs show a noticeably enhanced OER activity, while the LCO NSs exhibit negligible OER enhancement, demonstrating that the basal plane of De-LCO is inactive while other major surfaces are active for OER. (b) Tafel plots of these four samples. (c) Overpotential shifting comparison of LCO NSs and NPs before and after delithiation, respectively. (d) Normalized polarization curves of LCO NSs, De-LCO NSs, LCO NPs and De-LCO NPs; the inset is the electric double layer capacitance (EDLC) measurement curves of LCO NSs and NPs.

where we can observe that both LCO NSs and LCO NPs were inactive for OER with large overpotentials at 10 mA cm⁻² (~ 530 and 510 mV, respectively, denoted as η_{10}). The similar activities of LCO NSs and NPs are not entirely consistent with the simulation results because the LCO NSs cannot completely eliminate the active surfaces. After delithiation, the OER activity of the LCO NSs was slightly improved with an η_{10} value of ~ 500 mV, while the De-LCO NPs exhibited a dramatically decreased η_{10} (from 510 to 390 mV, Figure 3c). All four samples showed similar Tafel slopes (~ 60 mV dec⁻¹, Figure 3b), indicating similar kinetics of the water oxidation reaction. In addition, the long-term stability testing indicated that the most active De-LCO NPs were stable under OER conditions (Figure S8).

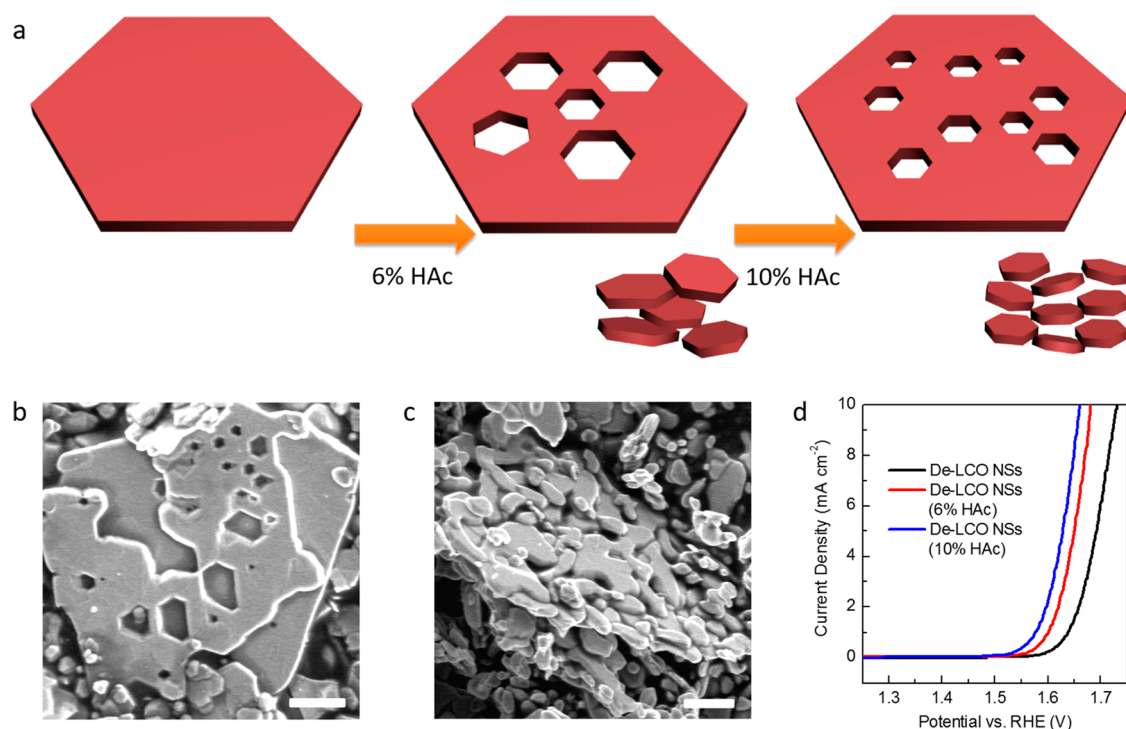


Figure 4. (a) Schematic illustration of the morphology evolution of LCO NSs after HAc etching at different concentrations; the LCO NSs would become more porous and the size of nanosheets would become smaller, suggesting that more active surfaces are exposed. (b, c) Representative SEM images of LCO NSs with 6% and 10% HAc etching, respectively. (d) OER polarization curves of De-LCO NSs and De-LCO NSs (6% HAc) and De-LCO NSs (10% HAc); the enhanced OER activity of De-LCO NSs after HAc etching indicates the intrinsically higher activities of generated surfaces.

The dissimilar sizes of LCO NSs and NPs may give rise to different surface areas, which also possibly contribute to the overall OER current.^{40–42} Thus, we have compared the surface area ratios of these two samples by measuring the electrochemical double layer capacitance (EDLC)¹⁴ of the pure catalyst (Figure S9). The results indicate that the LCO NPs possess a larger surface area than that of LCO NSs with a reasonable ratio of $\sim 1.37:1$ according to the EDLC (inset of Figure 3d). Brunauer–Emmett–Teller (BET) measurements suggested a similar surface area ratio ($\sim 1.15:1$) compared to the EDLC results. As the delithiated samples mostly inherited the pristine morphologies, we postulated that the surface area did not change dramatically. The normalized OER polarization curves (according to the EDLC results) were shown in Figure 3d, where we could observe that the OER activities of LCO NPs and NSs were basically the same, while that of the De-LCO NPs was still much better than that of De-LCO NSs. These electrochemical experiments and the aforementioned structural characterizations suggest that the (0001) of LCO is inactive, while other surfaces such as (01 $\bar{1}2$) and (11 $\bar{2}0$) are active for OER after electrochemical tuning.

From the above analysis, we reason that OER activity of De-LCO should improve if more active surfaces are exposed. To verify this hypothesis, we employed an acid etching method on LCO NSs to create more active surfaces and subsequently investigated the OER enhancement. SEM images (Figures 4b and S10) showed that the size of LCO NSs becomes smaller ($\sim 1 \mu\text{m}$) and several quasi-hexagonal holes appear in the occasionally large LCO NSs after immersing in a certain concentration ($\sim 6\%$) of HAc solution overnight. According to the morphology evolution, we can reasonably hypothesize that the total area of basal plane negligibly changes while more

active surfaces are generated,²⁷ as is schematically shown in Figure 4a. Moreover, an even smaller size as well as a much higher porosity on large LCO NSs was observed if a higher concentration of HAc solution ($\sim 10\%$) was adopted, indicating an increased concentration of active surfaces (Figure 4c). XRD patterns (Figure S11) shows that the crystallinity of LCO NSs with HAc etching became much weaker while the (0001) plane was still the preferentially exposed surface. As expected, the OER activities of the acid-etched De-LCO NSs were both improved, lowering the η_{10} value to ~ 450 and ~ 430 mV for the De-LCO NSs etched with 6% and 10% HAc, respectively. This experimental observation further confirms that the active surfaces of De-LCO for OER are other surfaces rather than the (0001) and also proposes an effective etching method for further improving the electrocatalytic activity.

CONCLUSIONS

In summary, the OER active surfaces for LCO before and after the delithiation process were determined from both theoretical and experimental perspectives. Theoretical simulation results indicate that the most stable (0001) surface shows quite large overpotential for OER independent of the level of lithiation. However, other surfaces such as the polar (01 $\bar{1}2$) and the nonpolar (11 $\bar{2}0$) surfaces are identified to be active, and they can be further activated by delithiation. The reduced overpotentials of these surfaces come from better $\Delta G_{\text{O}} - \Delta G_{\text{OH}}$ energetics. This effect can be attributed to the increase of the number of Co^{4+} sites and its strong covalent coupling to oxygen 2p states. In our experiment, a morphology-control strategy was employed to understand the fundamental role of electrochemical tuning as well as identify the active surfaces of LCO/De-LCO system. It is found that the significant OER

enhancement directed by electrochemical delithiation can only be observed on LCO NPs and not in the LCO NSs, and this difference can originate from the greater distribution of more active OER surfaces on LCO NPs. The relationship between the active surfaces and the OER activity was further studied by employing an acid etching process on LCO NSs, where more active surfaces were exposed and the corresponding OER activity was enhanced. This study provides a useful strategy for determining the active surfaces, which is of important significance for guiding the rational design of advanced OER catalysts.

THEORETICAL SECTION

Computational Details. We have performed DFT+U calculations within the Vienna ab initio simulation package^{43,44} (VASP) using the projector augmented wave (PAW) potentials.⁴⁵ We adapt the PBE⁴⁶ functional together with the Hubbard-*U* method⁴⁷ applied for the *d*-electrons of Co atoms. The value of the effective Hubbard-*U* parameter, $U_{\text{eff}} = 3.32$ eV, is taken from previous works on cobalt oxides.^{27,48,49} The bulk optimization calculations were performed on the $8 \times 8 \times 6$ k-point mesh per $1 \times 1 \times 1$ unit-cell of LCO and energy cutoff of 800 eV. The application of this method to bulk LCO results in the optimized lattice constants $a = 2.834$ Å and $z = 14.158$ Å (exp. values:⁵⁰ $a = 2.816$ and $c = 14.054$), optical band gap $E_g = 2.0$ eV (exp. values 2.1–2.4 eV), and a zero magnetic moment on the Co ions. The calculated low-spin Co^{3+} corresponds to a well-known fully occupied t_{2g} bands in octahedral crystal field splitting. The 50% Li removal leads to well-known elongation allowing the *z*-direction with optimized lattice constants $a = 2.816$ Å and $z = 14.610$ Å (exp. values:⁵⁰ $a = 2.809$ and $c = 14.389$) also observed by number of studies.^{31,34,50} For surfaces, we have employed symmetric slabs of 6 or more layers with minimum of 15 Å of vacuum, and to achieve the maximum error cancellation, the same unit-cell shapes were used for LCO and $\text{Li}_{0.5}\text{CoO}_2$ surfaces. Here we used similar $8 \times 8 \times 1$ k-point mesh per surface Co atom and energy cutoff of 400 eV (increasing the cutoff to 550 eV led to less than 0.05 eV change in the calculated adsorption energies). Both clean slabs and slabs with symmetric adsorbates on both sides were always fully relaxed below minimum threshold force of 0.05 eV/Å². Finally, to obtain the theoretical overpotential (eq 1) for each surface, the Gibbs free energies of the OER intermediates were calculated at room temperature by adding the potential energy, the zero point energy (ZPE), and the vibrational enthalpy and entropy contributions obtained by means of the harmonic approximation.

EXPERIMENTAL SECTION

Synthesis of LCO NSs and NPs. The LCO NSs and NPs were both fabricated by a hydrothermal reaction followed by a calcination process.³⁶ For LCO NSs, we first synthesized $\text{Co}(\text{OH})_2$ nanosheets as precursor by a modified method reported previously. Briefly, 2 mmol of $\text{CoCl}_2 \cdot 6\text{H}_2\text{O}$ and 10 mmol of hexamethylenetetramine (HMT) were dissolved in 36 mL of H_2O , which was stirred to form a clear solution. The aqueous solution was subsequently transferred to a 40 mL Teflon-lined stainless-steel autoclave, which was sealed, maintained at 120 °C for 2 h, and then allowed to cool to room temperature naturally. Afterward, the resulting powder was isolated by centrifugation, washed three times with water, and then dried in an oven under 80 °C overnight. The LCO NSs can be obtained by simply mixing the as-prepared $\text{Co}(\text{OH})_2$ with $\text{LiOH} \cdot \text{H}_2\text{O}$ and calcining the mixture at 800 °C for 4 h. The LCO NPs were synthesized by a similar procedure. We used $\text{CoCl}_2 \cdot 6\text{H}_2\text{O}$ (4 mmol) and urea (5 mmol) as the raw materials in the hydrothermal step (120 °C for 5 h) to fabricate $\text{Co}_2(\text{OH})_2\text{CO}_3$ nanowire precursor, which was then transformed into Co_3O_4 nanowires by heating at 500 °C for 3 h. The dark product was mixed with $\text{LiOH} \cdot \text{H}_2\text{O}$ and calcined at 800 °C for 3 h to obtain LCO NPs.

Electrochemical Tuning Process of LCO. The electrochemical tuning process was similar to the procedure previously reported.²⁶ First the slurries containing ~80% active material, ~15% conducting

carbon black, and ~5% PVDF binder were first made in an ethanol solvent. Then the slurries were doctor-bladed onto aluminum foil and dried at 50 °C overnight. Afterward, the electrodes (aluminum foil covered by slurries) were cut out and put into pouch cells, which were assembled in an argon-filled glovebox free of oxygen and water. The negative electrode was lithium metal foil, and the electrolyte we use was a 1 M solution of LiPF_6 in ethylene carbonate and diethyl carbonate (EC/DEC, 1:1, from Ferro Corporation). The separator was polypropylene-based Celgard 2321. The electrochemical tuning process was performed by charging the cell to 4.3 V vs Li^+/Li after one charge/discharge cycle. Consequently, the delithiated product was taken out and rinsed with ethanol several times.

Structural Characterizations. The size and morphology of LCO NSs and NPs were carried out using scanning electron microscopy (SEM, FEI Nova NanoSEM 450) and high-resolution transmission electron microscopy (HRTEM, FEI Titan). The X-ray powder diffraction patterns were recorded on an X-ray diffractometer (Rigaku D/max 2500) in the range from 15° to 80°.

Electrochemical Characterizations. The catalyst inks were prepared containing ~80% of the catalyst, ~15% of additive carbon, and ~5% of PVDF in ethanol solution to achieve a catalyst concentration of ~1 mg·mL⁻¹. For the LCO ink preparation, these components were added manually, while the De-LCO ink could be prepared by directly dispersing the mixture after delithiation in ethanol. After sonicating for 45 min, 100 μL of the catalyst ink was drop-dried onto a 1 cm × 1 cm carbon fiber paper (from Fuel Cell Store, the mass loading was ~0.1 mg·cm⁻²). The OER measurements were performed in 0.1 M KOH (pH = 13) solution using a three electrode setup, with a SCE reference electrode and a platinum wire counter electrode. The reference electrode was calibrated in H_2 saturated electrolyte with respect to an in situ reverse hydrogen electrode (RHE), yielding the relation $E(\text{RHE}) = E(\text{SCE}) + 0.99$ V. The electrode was first cycled ~5 times by cyclic voltammetry (CV) until a stable CV curve was developed before measuring polarization curves. Linear sweep voltammetry (scan rate of 2 mV·s⁻¹) and AC impedance spectroscopy (at zero overpotential) were recorded by a Biologic VSP potentiostat. The EDLC measurements were conducted in the potential range of 1.25 to 1.30 V vs RHE, where no Faradaic reaction occurred.

ASSOCIATED CONTENT

Supporting Information

The Supporting Information is available free of charge on the ACS Publications website at DOI: 10.1021/jacs.7b02622.

Intensity ratios of three surfaces for LCO NSs and NPs, OER activity comparisons of LCO NSs and LCO NPs before and after delithiation, surface Pourbaix diagrams of different LiCoO_2 and $\text{Li}_{0.5}\text{CoO}_2$ surfaces, calculated scaling between GOH and GOOH used to construct 2D contour plot of Figure 1, projected densities of states (PDOS) of optimized LiCoO_2 and $\text{Li}_{0.5}\text{CoO}_2$, PDOS plots for the Co active site and O* for all surfaces from Figure 1, typical charging curve of LCO NSs, representative SEM images of LCO NSs and LCO NPs before and after delithiation, stability testing of the most active De-LCO NPs for 10 h, CV curves of LCO NPs and LCO NSs, SEM images of LCO NSs with 6% and 10% HAc etching, and powder XRD patterns of LCO NSs, LCO NSs (6% HAc), and LCO NSs (10% HAc) (PDF)

AUTHOR INFORMATION

Corresponding Authors

*bajdich@slac.stanford.edu

*yicui@stanford.edu

ORCID 

Zhiyi Lu: 0000-0002-2117-4101

Yuzhang Li: 0000-0002-1502-7869

Alan C. Luntz: 0000-0002-1003-1914

Notes

The authors declare no competing financial interest.

ACKNOWLEDGMENTS

This work was initiated by the support of the Department of Energy, Office of Basic Energy Sciences, Materials Sciences and Engineering Division, under contract DEAC02-76-SFO0515. We acknowledge support from the Global Climate Energy Projects at Stanford University and SUNCAT seed funding in SLAC.

REFERENCES

- (1) Novoselov, K. S.; Geim, A. K.; Morozov, S. V.; Jiang, D.; Zhang, Y.; Dubonos, S. V.; Grigorieva, I. V.; Firsov, A. A. *Science* **2004**, *306*, 666.
- (2) Geim, A. K.; Novoselov, K. S. *Nat. Mater.* **2007**, *6*, 183.
- (3) Li, X.; Wang, X.; Zhang, L.; Lee, S.; Dai, H. *Science* **2008**, *319*, 1229.
- (4) Radisavljevic, B.; Radenovic, A.; Brivio, J.; Giacometti, i. V.; Kis, A. *Nat. Nanotechnol.* **2011**, *6*, 147.
- (5) Wang, Q. H.; Kalantar-Zadeh, K.; Kis, A.; Coleman, J. N.; Strano, M. S. *Nat. Nanotechnol.* **2012**, *7*, 699.
- (6) Wang, H.; Yuan, H.; Hong, S. S.; Li, Y.; Cui, Y. *Chem. Soc. Rev.* **2015**, *44*, 2664.
- (7) Wang, H.; Zhang, Q.; Yao, H.; Liang, Z.; Lee, H.-W.; Hsu, P.-C.; Zheng, G.; Cui, Y. *Nano Lett.* **2014**, *14*, 7138.
- (8) Chhowalla, M.; Shin, H. S.; Eda, G.; Li, L.-J.; Loh, K. P.; Zhang, H. *Nat. Chem.* **2013**, *5*, 263.
- (9) Wu, W.; Wang, L.; Li, Y.; Zhang, F.; Lin, L.; Niu, S.; Chenet, D.; Zhang, X.; Hao, Y.; Heinz, T. F.; et al. *Nature* **2014**, *514*, 470.
- (10) Hinnemann, B.; Moses, P. G.; Bonde, J.; Jørgensen, K. P.; Nielsen, J. H.; Horch, S.; Chorkendorff, I.; Nørskov, J. K. *J. Am. Chem. Soc.* **2005**, *127*, 5308.
- (11) Jaramillo, T. F.; Jørgensen, K. P.; Bonde, J.; Nielsen, J. H.; Horch, S.; Chorkendorff, I. *Science* **2007**, *317*, 100.
- (12) Louie, M. W.; Bell, A. T. *J. Am. Chem. Soc.* **2013**, *135*, 12329.
- (13) Yeo, B. S.; Bell, A. T. *J. Am. Chem. Soc.* **2011**, *133*, 5587.
- (14) McCrory, C. C.; Jung, S.; Peters, J. C.; Jaramillo, T. F. *J. Am. Chem. Soc.* **2013**, *135*, 16977.
- (15) Zhang, Y.; Ding, F.; Deng, C.; Zhen, S.; Li, X.; Xue, Y.; Yan, Y.-M.; Sun, K. *Catal. Commun.* **2015**, *67*, 78.
- (16) Bajdich, M.; García-Mota, M.; Vojvodic, A.; Nørskov, J. K.; Bell, A. T. *J. Am. Chem. Soc.* **2013**, *135*, 13521.
- (17) Friebe, D.; Louie, M. W.; Bajdich, M.; Sanwald, K. E.; Cai, Y.; Wise, A. M.; Cheng, M.-J.; Sokaras, D.; Weng, T.-C.; Alonso-Mori, R.; et al. *J. Am. Chem. Soc.* **2015**, *137*, 1305.
- (18) Li, Y.-F.; Selloni, A. *ACS Catal.* **2014**, *4*, 1148.
- (19) Stoerzinger, K. A.; Choi, W. S.; Jeon, H.; Lee, H. N.; Shao-Horn, Y. *J. Phys. Chem. Lett.* **2015**, *6*, 487.
- (20) Petrie, J. R.; Jeon, H.; Barron, S. C.; Meyer, T. L.; Lee, H. N. *J. Am. Chem. Soc.* **2016**, *138*, 7252.
- (21) Wang, H.; Lu, Z.; Xu, S.; Kong, D.; Cha, J. J.; Zheng, G.; Hsu, P.-C.; Yan, K.; Bradshaw, D.; Prinz, F. B.; Cui, Y. *Proc. Natl. Acad. Sci. U. S. A.* **2013**, *110*, 19701.
- (22) Wang, H.; Lu, Z.; Kong, D.; Sun, J.; Hymel, T. M.; Cui, Y. *ACS Nano* **2014**, *8*, 4940.
- (23) Wang, H.; Lee, H.-W.; Deng, Y.; Lu, Z.; Hsu, P.-C.; Liu, Y.; Lin, D.; Cui, Y. *Nat. Commun.* **2015**, *6*, 7261.
- (24) Liu, Y.; Wang, H.; Lin, D.; Liu, C.; Hsu, P.-C.; Liu, W.; Chen, W.; Cui, Y. *Energy Environ. Sci.* **2015**, *8*, 1719.
- (25) Wang, H.; Xu, S.; Tsai, C.; Li, Y.; Liu, C.; Zhao, J.; Liu, Y.; Yuan, H.; Abild-Pedersen, F.; Prinz, F. B.; et al. *Science* **2016**, *354*, 1031.
- (26) Lu, Z.; Wang, H.; Kong, D.; Yan, K.; Hsu, P.-C.; Zheng, G.; Yao, H.; Liang, Z.; Sun, X.; Cui, Y. *Nat. Commun.* **2014**, *5*, 4345.
- (27) Kramer, D.; Ceder, G. *Chem. Mater.* **2009**, *21*, 3799.
- (28) Nørskov, J. K.; Rossmeisl, J.; Logadottir, A.; Lindqvist, L.; Kitchin, J. R.; Bligaard, T.; Jonsson, H. *J. Phys. Chem. B* **2004**, *108*, 17886.
- (29) Dionigi, F.; Strasser, P. *Adv. Energy Mater.* **2016**, *6*, 1600621.
- (30) Laubach, S.; Laubach, S.; Schmidt, P. C.; Ensling, D.; Schmid, S.; Jaegermann, W.; Thißen, A.; Nikolowski, K.; Ehrenberg, H. *Phys. Chem. Chem. Phys.* **2009**, *11*, 3278.
- (31) Xiong, F.; Yan, H.; Chen, Y.; Xu, B.; Le, J.; Ouyang, C. *Int. J. Electrochem. Sci.* **2012**, *7*, 9390.
- (32) Aydinol, M.; Kohan, A.; Ceder, G.; Cho, K.; Joannopoulos, J. *Phys. Rev. B: Condens. Matter Mater. Phys.* **1997**, *56*, 1354.
- (33) Ensling, D.; Cherkashinin, G.; Schmid, S.; Bhuvanawari, S.; Thissen, A.; Jaegermann, W. *Chem. Mater.* **2014**, *26*, 3948.
- (34) Laubach, S.; Laubach, S.; Schmidt, P. C.; Ensling, D.; Schmid, S.; Jaegermann, W.; Thißen, A.; Nikolowski, K.; Ehrenberg, H. *Phys. Chem. Chem. Phys.* **2009**, *11*, 3278.
- (35) Graetz, J.; Hightower, A.; Ahn, C.; Yazami, R.; Rez, P.; Fultz, B. *J. Phys. Chem. B* **2002**, *106*, 1286.
- (36) Xiao, X.; Liu, X.; Wang, L.; Zhao, H.; Hu, Z.; He, X.; Li, Y. *Nano Res.* **2012**, *5*, 395.
- (37) Qian, X.; Cheng, X.; Wang, Z.; Huang, X.; Guo, R.; Mao, D.; Chang, C.; Song, W. *Nanotechnology* **2009**, *20*, 115608.
- (38) Reimers, J. N.; Dahn, J. J. *Electrochem. Soc.* **1992**, *139*, 2091.
- (39) Takahashi, Y.; Kijima, N.; Tokiwa, K.; Watanabe, T.; Akimoto, J. *J. Phys.: Condens. Matter* **2007**, *19*, 436202.
- (40) Xu, J.; Aili, D.; Li, Q.; Christensen, E.; Jensen, J. O.; Zhang, W.; Hansen, M. K.; Liu, G.; Wang, X.; Bjerrum, N. J. *Energy Environ. Sci.* **2014**, *7*, 820.
- (41) Wang, J.; Zhong, H. x.; Qin, Y. l.; Zhang, X. b. *Angew. Chem.* **2013**, *125*, 5356.
- (42) Song, F.; Hu, X. *Nat. Commun.* **2014**, *5*, 4477.
- (43) Kresse, G.; Furthmüller, J. *Comput. Mater. Sci.* **1996**, *6*, 15.
- (44) Kresse, G.; Hafner, J. *Phys. Rev. B: Condens. Matter Mater. Phys.* **1993**, *47*, 558.
- (45) Kresse, G.; Joubert, D. *Phys. Rev. B: Condens. Matter Mater. Phys.* **1999**, *59*, 1758.
- (46) Perdew, J. P.; Burke, K.; Ernzerhof, M. *Phys. Rev. Lett.* **1996**, *77*, 3865.
- (47) Dudarev, S.; Botton, G.; Savrasov, S.; Humphreys, C.; Sutton, A. *Phys. Rev. B: Condens. Matter Mater. Phys.* **1998**, *57*, 1505.
- (48) García-Mota, M. n.; Bajdich, M.; Viswanathan, V.; Vojvodic, A.; Bell, A. T.; Nørskov, J. K. *J. Phys. Chem. C* **2012**, *116*, 21077.
- (49) Wang, L.; Maxisch, T.; Ceder, G. *Phys. Rev. B: Condens. Matter Mater. Phys.* **2006**, *73*, 195107.
- (50) Takahashi, Y.; Kijima, N.; Dokko, K.; Nishizawa, M.; Uchida, I.; Akimoto, J. *J. Solid State Chem.* **2007**, *180*, 313.